ARTICLE

Suppressing Dendrite Growth and Side Reactions via Mechanically Robust Laponite-Based Electrolyte Membranes for Ultrastable Aqueous Zinc-Ion Batteries

Siyu Tian, Taesoon Hwang, Yafen Tian, Yue Zhou, Long Zhou, Tye Milazzo, Seunghyun Moon, Sina Malakpour Estalaki, Shiwen Wu, Ruda Jian, Kenneth Balkus, Tengfei Luo, Kyeongjae Cho,* and Guoping Xiong*
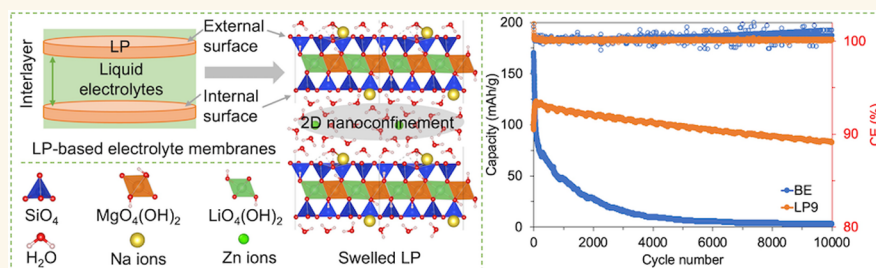
ACCESS | 📊 Metrics & More | 📰 Article Recommendations | 🆂�🅸 Supporting Information

ABSTRACT: The development of aqueous zinc-ion batteries (AZIBs) faces significant challenges because of water-induced side reactions arising from the high water activity in aqueous electrolytes. Herein, a quasi-solid-state electrolyte membrane with low water activity is designed based on a laponite (LP) nanoclay for separator-free AZIBs. The mechanically robust LP-based membrane can perform simultaneously as a separator and a quasi-solid-state electrolyte to inhibit dendrite growth and water-induced side reactions at the Zn/electrolyte interface. A combination of density functional theory calculations, theoretical analyses, and experiments ascertains that the water activities associated with self-dissociation, byproduct formation, and electrochemical decomposition could be substantially suppressed when the water molecules are absorbed by LP. This could be attributed to the high water adsorption and hydration capabilities of LP nanocrystals, resulting from the strong Coulombic and hydrogen-binding interactions between water and LP. Most importantly, the separator-free AZIBs exhibit high capacity retention rates of 94.10% after 2,000 cycles at 1 A/g and 86.32% after 10,000 cycles at 3 A/g, along with enhanced durability and record-low voltage decay rates over a 60-day storage period. This work provides a fundamental understanding of water activity and demonstrates that LP nanoclay is promising for ultrastable separator-free AZIBs for practical energy storage applications.

KEYWORDS: Laponite swelling nanoclay, Electrolytes, Separator-free, Water activity, Zn metal anodes, Aqueous zinc-ion batteries

1. INTRODUCTION

In the past few decades, tremendous efforts have been devoted to utilizing renewable energy resources such as wind and sunlight to address the worldwide energy crisis and global warming.[1] However, managing the intermittent power generated from these renewable energy devices remains challenging due to the lack of high-performance, low-cost, and high-safety grid-scale energy storage systems.[2] Recently, aqueous zinc-ion batteries (AZIBs) have emerged as promising candidates for

grid-scale energy storage applications due to their distinct advantages, including low-cost, eco-friendliness, high material
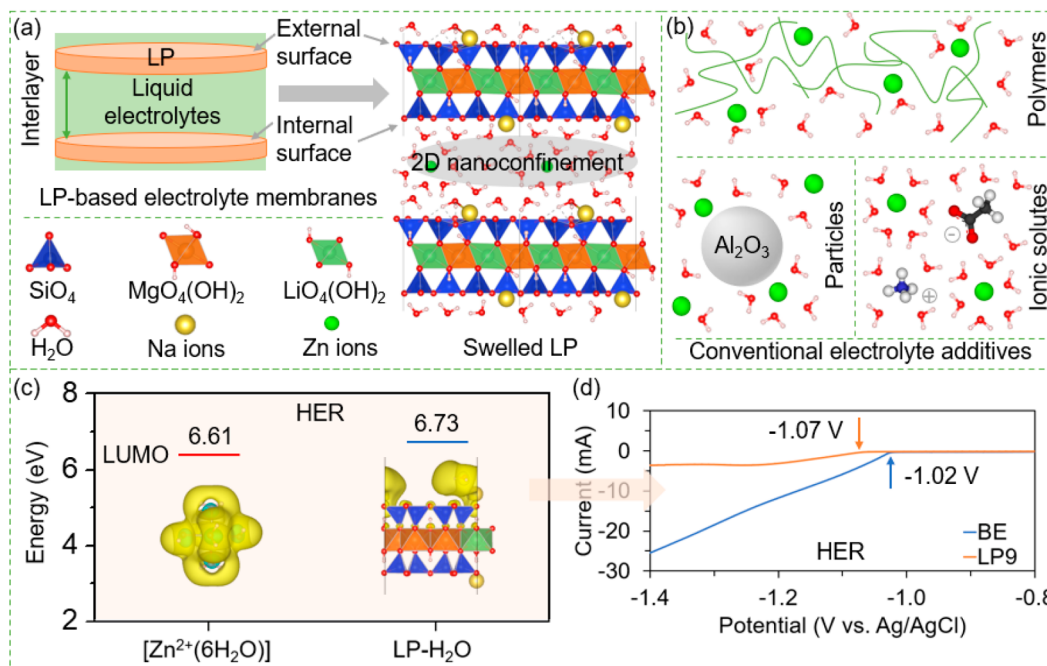
Figure 1. Schematic illustrations of (a) electrolyte membranes based on LP nanocrystals with 2D nanostructures and exceptional swelling capabilities and (b) conventional liquid electrolytes containing other additives, such as polymers (e.g., polyacrylamide[32]), inorganic particles (e.g., Al_2O_3[33]), and ionic solutes (e.g., ammonia acetate[34]). (c) LUMO energies of water molecules in BE and LP9 electrolyte membrane. (d) HER performance of Zn metal electrodes in BE and LP9 electrolyte membrane.

abundance, high theoretical capacity, and low safety risks.[3,4] Despite the recent progress in enhancing the electrochemical performance of AZIBs, their practical applications are still impeded by the poor cyclic stability and unsatisfactory durability arising from water-induced side reactions at the Zn/electrolyte interface. These undesirable side reactions, including hydrogen evolution, zinc corrosion, byproduct formation, and dendrite growth, severely impair the stability of the Zn/electrolyte interface, resulting in poor cyclic stability and unsatisfactory durability of AZIBs during long-term cycling or storage.[5,6]

In AZIBs, water plays a critical role in determining the physicochemical properties of electrolytes, electrode/electrolyte interfacial chemistries, and ultimately the electrochemical performance of batteries.[7] The main bottleneck of aqueous electrolytes is the narrow electrochemical stability window (ESW) of water, which is 1.23 V as determined by its thermodynamic oxidation (oxygen evolution reaction − OER) and reduction (hydrogen evolution reaction − HER) potentials.[8] In mild acidic electrolytes, such as zinc sulfate solutions, water molecules exhibit high activity due to the excess free water content and the self-dissociation ($H_2O \leftrightarrow H^+ + OH^-$) of free water molecules.[9] Therefore, spontaneous Zn corrosion and HER could easily occur at the Zn/electrolyte interface following the given reactions:[10,11]

$$Zn + 2H^+ \rightarrow Zn^{2+} + H_2\uparrow \qquad \text{Zn corrosion} \qquad (1)$$

$$2H^+ + 2e^- \rightarrow H_2\uparrow \qquad \text{HER} \qquad (2)$$

Notably, Zn corrosion and HER lead to irreversible electrolyte consumption, continuous water decomposition, uneven and porous Zn deposition, fast dendrite growth, and increased pH at the Zn/electrolyte interface. The localized high-pH environment further facilitates the formation of byproducts − zinc hydroxide sulfate hydrate (ZHS) − through the reaction:[12,13]

$$4Zn^{2+} + 6OH^- + SO_4^{2-} + xH_2O \rightarrow Zn_4(OH)_6SO_4 \cdot xH_2O$$

ZHS formation

$$(3)$$
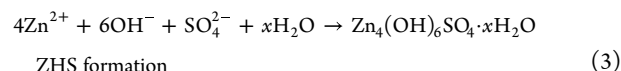
Different from the protective solid-electrolyte interphase (SEI) in lithium-ion batteries, the formation of ZHS cannot eliminate the occurrence of water-induced side reactions at the Zn/electrolyte interface, deteriorating the cyclic stability of AZIBs.[14] In addition, the ion- and electron-insulating ZHS passivates the active surface of Zn metal, leading to increased internal resistance and uneven Zn plating/stripping.[13] Therefore, understanding and regulating water activity to protect Zn metal anodes against water-induced side reactions are crucial for designing advanced aqueous electrolytes for highly stable AZIBs.

To date, extensive efforts have been made to regulate water activity and suppress water-induced side reactions at the Zn/electrolyte interface. Effective strategies that can enhance the cyclic stability of AZIBs include anode modification,[15−17] separator functionalization,[18] and electrolyte engineering.[19,20] From the perspective of water molecules, they exist in the bulk electrolyte phase or at the electrode/electrolyte interfaces. Moreover, regulating the water activity in aqueous electrolytes through additives has shown great potential to enhance the cyclic stability of AZIBs.[7,21] As summarized in Table S1, electrolyte additives, including organic molecules,[22−24] inorganic salts,[25−27] metal oxide particles,[28−30] and carbon materials,[31] have been added to the baseline electrolytes (e.g., 1−3 M $ZnSO_4$). However, the water activity and how it is affected by the additive-water interactions in these engineered electrolyte systems have not been thoroughly understood. Moreover, a high-cost glass fiber (GF) separator is frequently required for these electrolytes to ensure the operation of batteries, further mitigating the cost competitiveness of AZIBs and posing significant challenges for their large-scale implementation. Therefore, exploring more efficient electrolyte
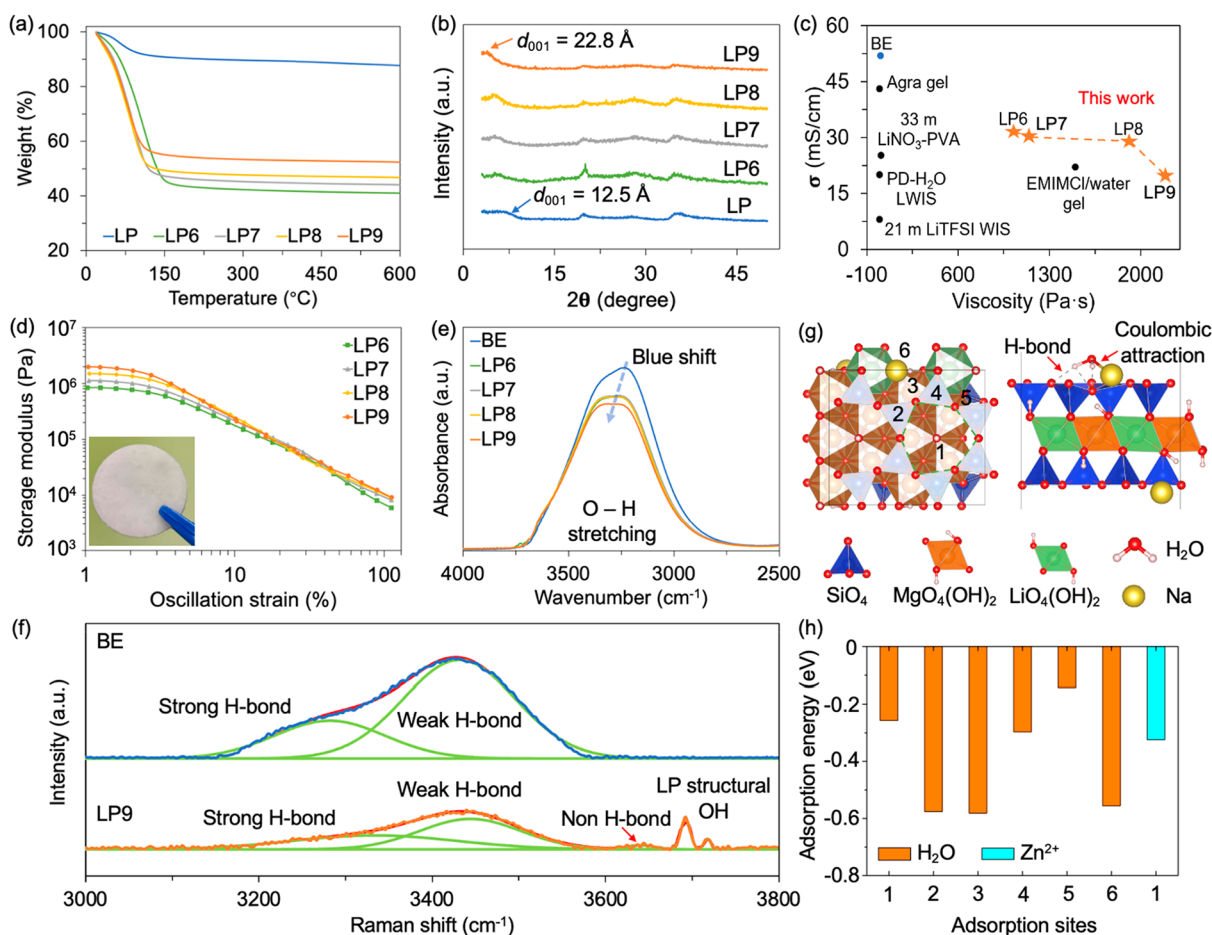
Figure 2. Physical and chemical properties of LP, BE, and LP-based electrolyte membranes. (a) TGA curves. (b) XRD curves. (c) Comparison of ionic conductivity and viscosity of the LP-based electrolyte membranes and other electrolyte systems: agar gel,[35] 33 m LiNO$_3$-PVA (where m is molality, mol/kg),[36] PD-H$_2$O LWIS,[37] 21 m LiTFSI,[38] and EMIMCl/water gel.[39] (d) Storage modulus; the inserted optical image shows the appearance of a freestanding LP9 electrolyte membrane. (e) FTIR spectra. (f) Raman spectra. (g) Atomic surface model and representative H$_2$O adsorption configurations of the LP nanocrystals. (h) H$_2$O and Zn^{2+} adsorption energies at different sites.

systems and understanding the ambiguous relationship between additive−water interactions and water activity are important to advance the development of AZIBs.

Herein, a freestanding, mechanically robust laponite (LP)-based electrolyte membrane with low water activity is rationally designed for ultrastable, separator-free AZIBs. As schematically illustrated in Figure 1a, the plate-like LP nanocrystals, with a trioctahedral 2:1 layered nanostructure and exceptional swelling capabilities, can absorb large amounts of water molecules and confine them on their external/internal surfaces and within the interlayers, thus significantly suppressing water activity and water-induced side reactions. Such an interlayer confinement phenomenon is significantly different from previously reported electrolyte systems containing conventional additives such as polymers, inorganic particles, and ionic solutes.[32−34] In these conventional electrolyte systems, no two-dimensional (2D) nanoconfinement effect on water molecules exists, as shown in Figure 1b. Moreover, the strong LP−water interactions play a key role in regulating the water activity in the LP-based electrolyte membranes. As shown in Figure 1c, density functional theory (DFT) calculations show that the lowest unoccupied molecular orbital (LUMO) energy level of the water molecules absorbed by LP nanocrystals is above that of water molecules in the baseline electrolyte (BE, 2 M ZnSO$_4$ in water). This observation implies enhanced electrochemical stability for

these adsorbed water molecules against electrochemical reduction (HER). Figure 1d further shows that the Zn metal electrode exhibits a delayed HER onset potential and a lower HER current in the optimal LP9 (i.e., 9 g of LP in 10 mL of BE) electrolyte membrane in comparison to BE. For instance, at a constant potential of −1.4 V vs. Ag/AgCl, the HER currents in BE and LP9 electrolytes are 25.3 and 3.6 mA, respectively. These results provide strong evidence that the HER activity could be significantly suppressed by confining water molecules on the external/internal surfaces of the LP nanocrystals. Therefore, the LP-based separator-free AZIB full cells exhibit excellent long-term cyclic stability and outstanding reliability during long-term storage, primarily due to the significantly suppressed water-induced side reactions and uniform Zn deposition. Particularly, the LP-based full cells exhibit high capacity retention rates of 94.10% after 2,000 cycles and 86.32% after 10,000 cycles at current densities of 1 and 3 A/g, respectively. The freestanding LP-based electrolyte membrane is demonstrated to be a promising candidate for fabricating cost-competitive, high-performance AZIBs.

2. RESULTS AND DISCUSSION

2.1. Electrolyte Characterization. Figure S1 and Figure S2 show the SEM image and X-ray photoelectron spectroscopy (XPS) spectrum of the LP powders, respectively. The LP

powders mainly consist of Si, Mg, Li, Na, and O elements, consistent with the empirical chemical formula of $Na^+_{0.7}$ $[Mg_{5.5}Li_{0.3}Si_8O_{20}(OH)_4]^{-0.7}$.[40] Such a 2:1 phyllosilicate nanoclay contains two magnesium octahedral layers and a sandwiched silica tetrahedral layer. The single LP nanocrystal possesses a diameter of 25 nm and a thickness of 0.92 nm.[41] In the LP nanocrystals, lithium partially substitutes magnesium atoms, resulting in a negatively charged basal plane, which is neutralized by interlayer sodium ions.[40] The electrolyte membranes with different amounts of LP are denoted as LPx, where x represents the mass of LP in 10 mL of BE. For instance, the electrolyte membranes with 6 and 9 g of LP in 10 mL of BE are denoted as LP6 and LP9, respectively. Note that the electrolyte membranes with lower concentrations of LP (e.g., LP5) are not sufficiently robust to function as a separator. Moreover, the separator-free LP9-based Zn∥NVO full cell exhibits superior stability over long-term cycling in comparison with other electrolyte membranes containing lower LP concentrations. At higher LP concentrations, such as LP10 electrolyte membrane, inadequate electrolyte-electrode wetting is observed, resulting in the low capacity of AZIB full cells, as shown in Figure S3.

Figure 2a and Figure S4 show the thermogravimetric analysis (TGA) curves and the water contents of LP-based electrolyte membranes, respectively. Compared to BE containing an excess amount (75.3 wt%) of water, the water content in LP9 electrolyte membrane decreases to 45.3 wt%. In addition, water molecules from the BE can intercalate into the interlayers and be absorbed on the internal surface of LP nanocrystals due to the hydration effect.[42] As shown in Figure 2b, the basal spacing (d_{001}) of LP nanocrystals increases from 12.5 to 22.8 Å in the LP9 electrolyte membrane. Since the layer thickness of LP nanocrystals is 9.2 Å,[40] the interlayer spacing of the LP nanocrystals increases from 3.3 Å in the initial state to 13.6 Å upon water intercalation (Figure S5). Based on the estimation (see details in the Experimental Section), approximately 30% of the free water in BE is confined within the interlayers of LP nanocrystals. Furthermore, Figure S6 shows that the LP powders possess a large surface area of 321.3 m^2/g, offering abundant adsorption sites for the effective immobilization of water molecules on their external surfaces. Additionally, the pH and salt concentration of the LP9 electrolyte membrane are measured to be 5.03 (Figure S7) and 1.48 M (Figure S8), respectively. Compared to BE, the addition of LP nanocrystals results in a slight increase of pH from 4.64 to 5.03 due to their weak alkalinity arising from proton adsorption.[43] Meanwhile, the pH of the LP-based electrolyte membranes only varies slightly because of the high LP concentrations.[44,45]

LP nanocrystals can form a stable gel structure when dispersed in water due to the strong electrostatic attractions between the negatively charged basal planes and the positively charged edges of the nanocrystals.[46,47] Figure S9 exhibits the surface and cross-sectional morphologies of the LP9 electrolyte membrane. Different from the highly porous structure of polymer-based hydrogels, the LP9 electrolyte membrane exhibits a dense structure without the presence of pores. As shown in Figure 2c, the LP9 electrolyte membrane possesses an ultrahigh viscosity of 2,191.7 Pa·s, which is 332 times greater than that (6.6 Pa·s) of the BE. Despite the substantially increased viscosity, the LP9 electrolyte membrane exhibits a high ionic conductivity of 19.6 mS/cm, albeit lower than that (51.9 mS/cm) of the BE, surpassing the performance of previously reported gel electrolytes and water-in-salt electro-

lytes.[36,37] Moreover, as shown in Figure S10, the LP9 electrolyte membrane exhibits a Zn^{2+} transference number of 0.76, higher than those of conventional liquid electrolytes.[49,50] This could be attributed to the 2D nanostructures and the highly negatively charged basal plane of the LP nanocrystals, which facilitate fast cation diffusion in the quasi-solid-state electrolyte membrane.[48,49,51] Figure 2d presents the storage modulus (G') of the LP-based electrolyte membranes, and the inserted optical image shows the appearance of a freestanding LP9 electrolyte membrane. Notably, the LP6 and LP9 electrolyte membranes exhibit high G' values of 0.8 and 2.0 MPa, respectively, signifying their exceptional mechanical resistance against Zn dendrite growth. The exceptional mechanical strength of the LP-based electrolyte membranes ensures their function as robust separators for their successful integration into separator-free AZIBs. These characteristics of LP make it promising for regulating water activity in aqueous batteries.

To investigate the interactions between LP and water, Fourier-transform infrared (FTIR) and Raman spectroscopy tests were conducted. Figure 2e displays the FTIR spectra of the BE and LP-based electrolyte membranes. A typical broad O−H stretching vibration peak ranging from 2,700 to 3,800 cm^{-1} is observed due to the presence of water molecules. Comparatively, the broad O−H stretching vibration peak of the LP-based electrolyte membranes exhibits a lower magnitude and is blue-shifted to higher wavenumbers, suggesting the formation of strong hydrogen bonds (H-bonds) between water and LP and the weakened H-bonds among water molecules.[52−54] Figure 2f further shows the comparative Raman spectra of the BE and LP9 electrolyte membrane. In the LP9 electrolyte membrane, the intensity of the O−H stretching vibration originating from water molecules is largely suppressed because of reduced free water content.[55] In addition, the convolution of the O−H stretching vibration peak indicates that the water molecules in the BE are dominated by strong and weak H-bonds, consistent with prior work.[56] In contrast, for the LP9 electrolyte membrane, new peaks appear, which could be attributed to the O−H stretching vibration of non-H-bound water molecules at 3,650 cm^{-1} and the vibrations of structural -OH of the LP nanocrystals in the range of 3,675–3,730 cm^{-1}. These results infer that the water molecules in the LP9 electrolyte membrane are strongly bound by LP nanocrystals, resulting in significantly suppressed water activity.[57,58]

To understand the interactions between LP and BE, DFT calculations were performed to investigate the H_2O and Zn^{2+} adsorption behaviors. Detailed atomic structures of the absorbed water molecules on the LP surface are presented in Figure S11. Figure 2g shows the adsorption sites on the LP surface and illustrates the strong interactions between LP and absorbed H_2O at site 3 near the sodium ion. Strong H-bonding interaction and Coulombic attraction exist between H_2O and LP due to the abundant oxygen and sodium ions on the LP surface, posing a strong confinement effect on water molecules and thus leading to their low activity. Figure 2h summarizes the adsorption energies of H_2O and Zn^{2+} at different sites. The H_2O adsorption energies are negative across the entire LP surface, indicating stable water adsorption. Furthermore, the water adsorption energies at sites 2, 3, and 6 close to the sodium cation are considerably lower (approximately −0.58 eV) than those at other adsorption sites, implying the significant role of sodium cations in the superior water-binding and hydration swelling capabilities of the LP nanocrystals. In contrast, Zn^{2+} adsorption is found to be stable only at site 1 due to the existence
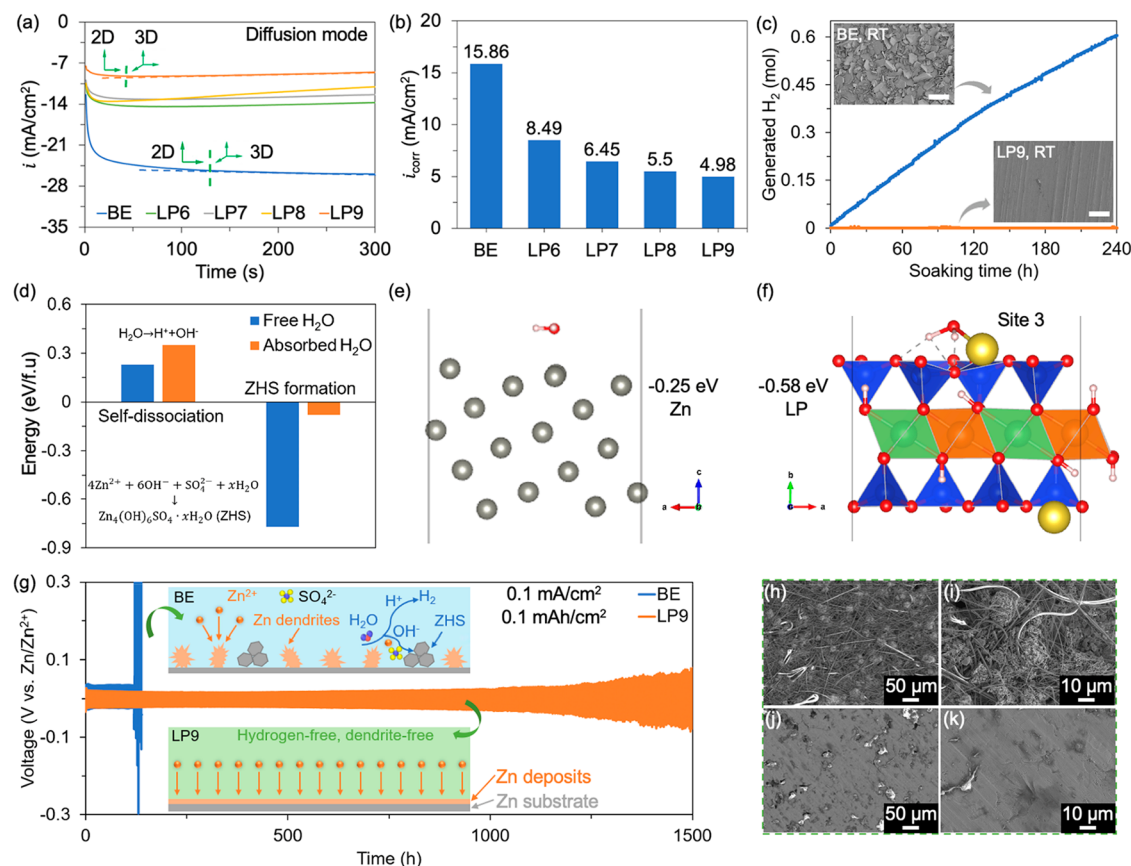
Figure 3. Electrochemical performance of Zn metal electrodes in BE and LP-based electrolyte membranes. (a) CA curves. (b) Corrosion current densities fitted from Tafel curves. (c) Hydrogen generation rates during the soaking tests (insets show the surface morphology of Zn foil after the soaking tests; scale bar: 50 μm). (d) Water self-dissociation and ZHS formation energies of free water molecules and absorbed water molecules on the LP surface. (e and f) Water adsorption energies on (e) Zn and (f) LP surfaces. (g) Long-term cycling performance of BE- and LP9-based Zn||Zn symmetric cells (insets schematically illustrate the Zn/electrolyte interfaces in BE and LP9 electrolyte membrane). (h−k) SEM images of Zn metal anodes in symmetric cells after 30 cycles at 1 mA/cm^2 and 1 mAh/cm^2 in different electrolytes: (h−i) BE with a GF separator and (j−k) LP9 electrolyte membrane.

of hexagonal-like voids formed by oxygen atoms. At other adsorption sites, Zn^{2+} adsorption is unstable because of the electrostatic repulsion between sodium and zinc cations (Figure S12). These results indicate that water molecules could be effectively confined by LP nanocrystals due to H-bonding interaction and Coulombic attraction, further suppressing water activity in LP-based electrolyte membranes and inhibiting water-induced side reactions at the Zn/electrolyte interface.

2.2. Water-Induced Side Reactions at the Zn/Electrolyte Interface. To investigate how water−LP interactions affect water-induced side reactions at the Zn/electrolyte interface, electrochemical tests of the Zn metal electrodes were conducted in different electrolytes. Figure 3a shows the chronoamperometry (CA) curves of the Zn metal electrodes in different electrolytes. The current density experiences a rapid increase during the initial 120 s in the BE, indicating a prolonged 2D diffusion process attributed to the inhomogeneous Zn nucleation and fast dendrite growth.[59] In the LP9 electrolyte membrane, Zn plating is dominated by 3D diffusion, leading to uniform and dense Zn deposition.[60] Therefore, the current density reaches equilibrium in 35 s and remains nearly constant throughout the subsequent galvanizing process. To investigate the Zn plating/stripping reversibility, Cu||Zn half cells were assembled and cycled at a current density of 1 mA/cm^2. Figure S13 and Figure S14 show the Coulombic efficiency and

nucleation overpotential of the BE- and LP9-based Cu||Zn half cells, respectively. The BE-based Cu||Zn half cell quickly fails after approximately 60 cycles and possesses a high nucleation overpotential of 41 mV. In comparison, the separator-free LP9-based Cu||Zn half cell exhibits an average CE of 99.6% over 150 cycles. Moreover, the nucleation overpotential significantly decreases to 11 mV, which could be attributed to the uniform Zn nucleation/deposition facilitated by the LP9 electrolyte membrane.[61,62] Figure 3b and Figure S15 exhibit the corrosion performance of Zn metal electrodes evaluated by Tafel tests. The corrosion current densities (i_{corr}) of Zn metal electrodes in BE and LP9 electrolyte are 15.86 and 4.96 mA/cm^2, respectively. Meanwhile, the corrosion potential (E_{corr}) in the LP9 electrolyte increases to −1.01 V. The lower i_{corr} and higher E_{corr} in the LP9 electrolyte indicate that Zn corrosion is considerably inhibited compared to that in BE. These results strongly support that water-induced side reactions and dendrite growth at the Zn/electrolyte interface could be effectively inhibited in the LP9 electrolyte membrane.

To further investigate the corrosion performance and HER activity, soaking tests were performed by immersing a large piece of Zn foil in BE and LP9 electrolytes. During the entire soaking process, the mass of the sample is monitored by using an analytical balance to calculate the hydrogen generation rates (see details in the Experimental Section). As shown in Figure 3c,

the hydrogen generation in BE reaches a rate of 28.32 μmol/(h·cm^2) or 0.68 mL/(h·cm^2). Meanwhile, large amounts of ZHS flakes are observed on the Zn surface, resulting from Zn corrosion and byproduct formation. In sharp contrast, no hydrogen evolution is detected in the LP9 electrolyte, and the Zn surface remains nearly the same as that (Figure S16) of the pristine Zn foil. Even at an elevated temperature of 50°C, the Zn foil embedded in the LP9 electrolyte membrane displays a flat and nearly byproduct-free surface after 10 days, as evidenced by the SEM images and XRD patterns shown in Figure S17 and Figure S18, respectively. In contrast, the Zn foil is heavily covered by large ZHS plates when immersed in BE under the same conditions, indicating that water-induced side reactions in BE are accelerated at an elevated temperature.

Figure 3d shows the water self-dissociation energies and the ZHS formation energies calculated by DFT considering that the water molecules are in a free state or are absorbed by LP nanocrystals. The self-dissociation energy of the water molecules confined by LP increases to 0.35 eV, higher than that (0.23 eV) of the free water molecules, which suggests that the water self-dissociation rate could be largely suppressed by LP because of strong water−LP interactions. In addition, the free water molecules are more favorable for ZHS formation with a low reaction energy of −0.77 eV. When the water molecules are absorbed by LP nanocrystals, the associated ZHS formation energy significantly increases to −0.08 eV, implying a substantially suppressed ZHS formation kinetics in the LP-based electrolyte membranes. Figure 3e and Figure 3f further exhibit the water adsorption energies on the Zn metal and LP surfaces, respectively. The water molecules are preferentially absorbed by LP nanocrystals with a lower water adsorption energy of −0.58 eV compared with that (−0.25 eV) for absorption on the Zn metal surface. These results demonstrate that the strong LP−water interactions play a decisive role in lowering the water activities related to self-dissociation and byproduct formation.

For characterizing the hydrogen evolution behavior, the HER overpotential (η) in aqueous electrolytes can be calculated by the Nernst equation:[63]

$$\eta = E_{H_2O/H_2} - E^{\ominus}_{H_2O/H_2}$$
$$= 2.303\frac{RT}{F}[\log_{10}(\alpha_{H_2O}) + 14 - pH] \qquad (4)$$

where α denotes the activity, E represents the potential, $E^{\ominus}$ refers to the standard potential, R is the gas constant, T is the temperature, and F is the Faraday constant. At a constant temperature and pH, the water activity in the LP-based electrolytes determines the HER behavior. In an ideal aqueous solution, the water activity α_{H_2O} is related to the molar fraction x_1 and activity coefficient γ_1 of the water molecules:[64]

$$\ln[(\alpha_{H_2O})^{ideal}] = \ln(x_1\gamma_1) \qquad (5)$$

For an ideal aqueous solution, the activity coefficient of water is unity.[64] Therefore, the water activity is determined solely by its concentration. For instance, in the LP9 electrolyte membrane, the water (45.3 wt%, Figure 2a) and proton (pH = 5.03, Figure S7) concentrations are lower than those of the BE, leading to decreased water activity and higher HER overpotential. Moreover, the strong interactions between LP and water can further lower the water activity in LP-based electrolyte membranes, according to the hydrate theory proposed by

Scatchard.[65,66] In a nonideal aqueous solution that considers solute−water interactions, water activity is correlated to solute hydration following the given equation:[64]

$$\ln(\alpha_{H_2O}; \text{hydration}) = -n_j/(n^{\circ}_{H_2O} - hn_j) \qquad (6)$$

where α_{H_2O} represents the water activity considering solute hydration, n_j is the molarity of solute j, $n^{\circ}_{H_2O}$ denotes the molarity of water under ideal conditions, and h is the hydration number of the solute. In eq 6, hn_j quantifies the water content that could be confined by the solute because of solute−water interactions. In LP-based electrolyte membranes, the LP nanocrystals with exceptional water-binding and hydration swelling capabilities can absorb significant amounts of water from the free water phase, attributed to the strong water−LP interactions as revealed by DFT calculations. Although the characterization of the exact hydration number remains rather challenging, the high hydration capability and low water adsorption energies strongly support that LP nanocrystals have a high h, resulting in the low water activity and high HER overpotential (η) of the LP9 electrolyte membrane. Consequently, the HER of Zn metal electrodes in the LP9 electrolyte membrane could be significantly suppressed. These analyses highlight that finding electrolyte additives (e.g., LP) with high hydration capability and low water adsorption energy can be the key to designing advanced aqueous electrolytes for next-generation high-performance AZIBs.

To investigate the effectiveness of the LP-based electrolyte membranes, Zn‖Zn symmetric cells were assembled and cycled at different current densities and areal capacities. As shown in Figure S19, the separator-free LP-based Zn‖Zn symmetric cells exhibit prolonged cycle life with increasing LP content at a current density of 1 mA/cm^2 and an areal capacity of 1 mAh/cm^2. Figure 3g further demonstrates that the cycle life of the LP9-based Zn‖Zn symmetric cell could be extended to 1,500 h at a lower current density of 0.1 mA/cm^2 and an areal capacity of 0.1 mAh/cm^2, indicating significantly enhanced Zn plating/stripping reversibility. The failure of the LP9-based Zn‖Zn symmetric cell due to increased polarization could be ascribed to the accumulation of slight irreversible reactions (e.g., ZHS formation) at the Zn/electrolyte interface. These side reactions gradually deteriorate the interfacial contact and impair charge transfer kinetics, leading to increased voltage polarization during Zn plating/stripping.[67] As shown in Figure 3h−i, considerable mossy, porous Zn deposits with embedded glass fibers originating from the GF separator are evident on the surface of the Zn metal anode after 30 cycles in the BE. The presence of the two diffraction peaks at 12.2° and 24.6° (Figure S20) indicates the formation of ZHS byproducts, stemming from the side reactions between Zn metal and active water molecules in the BE during long-term cycling. In contrast, the Zn metal anode paired with the LP9 electrolyte membrane exhibits an even and dendrite-free surface after cycling (Figure 3j−k). Moreover, only a minor diffraction peak at 12.2° (Figure S20) is observed due to the reduced water activity in the LP9 electrolyte membrane, confirming the effective inhibition of water-induced side reactions.

The inserted schematics in Figure 3g illustrate the Zn deposition mechanisms in the BE and LP9 electrolyte membrane. Due to the uneven Zn nucleation and deposition in the BE with a GF separator, considerable amounts of Zn dendrites form on the surface of Zn metal anodes. Additionally, the protons (H$^+$) originating from water self-dissociation react
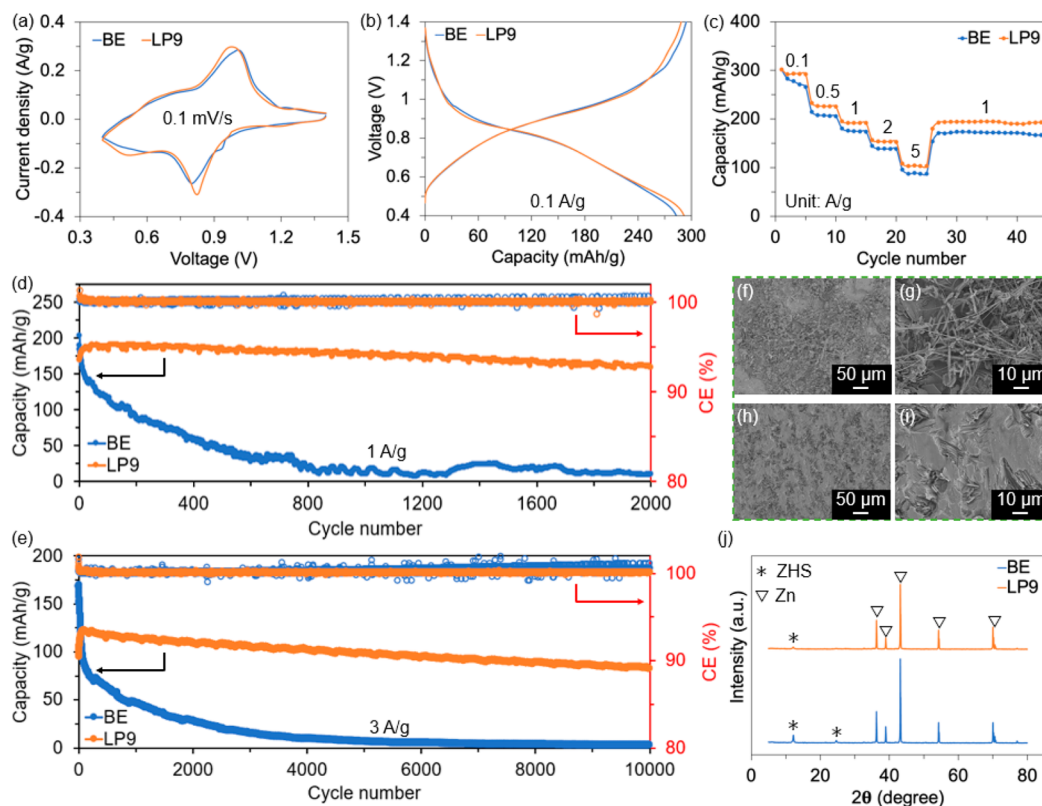
Figure 4. Electrochemical performance of BE- and LP9-based Zn‖NVO full cells: (a) CV curves. (b) Charge/discharge voltage profiles. (c) Rate performance. (d−e) Long-term cycling performance at (d) 1 A/g and (e) 3 A/g. (f−i) SEM images of Zn metal anodes after 1,000 cycles at 3 A/g in (f−g) the BE-based Zn‖NVO full cell with GF separator and (h−i) the separator-free LP9-based Zn‖NVO full cell. (j) XRD curves of Zn metal anodes in Zn‖NVO full cells after 1,000 cycles at 3 A/g.

with Zn metal and undergo electrochemical reduction, resulting in severe Zn corrosion and HER during Zn plating/stripping. The consumption of H⁺ increases the local OH⁻ concentration, further promoting the formation of ZHS byproducts at the Zn/electrolyte interface. Consequently, the reversibility of Zn metal anodes is severely deteriorated by water-induced side reactions in the BE. In contrast, the LP9 electrolyte membrane with low water activity can diminish interfacial instabilities by inhibiting Zn dendrite growth and water-induced side reactions, including hydrogen evolution, Zn corrosion, and byproduct formation due to the strong water−LP interactions. Therefore, highly reversible Zn metal anodes could be achieved when integrated with the freestanding LP9 electrolyte membrane.

2.3. Electrochemical Performance of the Separator-Free Zn‖NVO Full Cell. To demonstrate the advantages of the LP9 electrolyte membrane for practical applications, full cells were assembled and evaluated under different conditions. Sodium-doped vanadium oxide (NVO) was used as the cathode material, which has been widely reported in prior work.[68] Figure S21 displays the cycling performance of the LP9-based Zn‖NVO full cells with different electrolyte volumes. The full cell with an electrolyte volume of 100 μL exhibits optimal electrochemical performance, including a high capacity and excellent cyclic stability. In comparison to BE-based batteries, the volumetric energy density of the LP9-based Zn‖NVO full cells is expected to be higher due to the absence of GF separators. Meanwhile, the LP9 electrolyte membrane exhibits a higher density of 1.63 g/cm³ than that (1.31 g/cm³) of the BE, which slightly decreases the gravimetric energy density of the LP9-based batteries.

However, such a decrease is compensated by the removal of GF separators. Figure 4a and b present the cyclic voltammetry (CV) and galvanostatic charge/discharge curves of the BE- and LP9-based Zn‖NVO full cells, respectively. Compared with the BE-based batteries, the LP9-based Zn‖NVO full cells exhibit similar redox peaks and charge/discharge voltage profiles, suggesting that no extra redox reactions or parasitic reactions are introduced by LP. Figure 4c shows the rate capabilities of the BE- and LP9-based Zn‖NVO full cells. At current densities of 0.1, 0.5, 1, 2, and 5 A/g, the LP9-based Zn‖NVO full cell exhibits discharge capacities of 302.0, 232.9, 195.3, 156.7, and 108.4 mAh/g, respectively. When the current density is changed from 5 to 1 A/g, the LP9-based Zn‖NVO full cell maintains a discharge capacity of 192.8 mAh/g, higher than that (170.8 mAh/g) of the BE-based cell. This improvement could be attributed to the enhanced reversibility of the Zn metal anode in the LP9-based cell.

The long-term cyclic stability of the LP9-based full cells was further investigated at different current densities ranging from 0.1 to 3 A/g. As shown in Figure S22, the LP9-based Zn‖NVO full cell retains 70.65% of its initial capacity after 200 cycles at 0.1 A/g, much higher than that (22.11%) of the BE-based full cell. Figure 4d displays the cyclic stability of BE- and LP9-based Zn‖NVO full cells at a current density of 1 A/g. In sharp contrast to the BE-based full cell with fast capacity degradation, the LP9-based full cell exhibits substantially enhanced cyclic stability with a high capacity retention rate of 94.10% after 2,000 cycles. Figure 4e shows the cyclic stability of BE- and LP9-based Zn‖NVO full cells at a higher current density of 3 A/g. Notably, the LP9-based
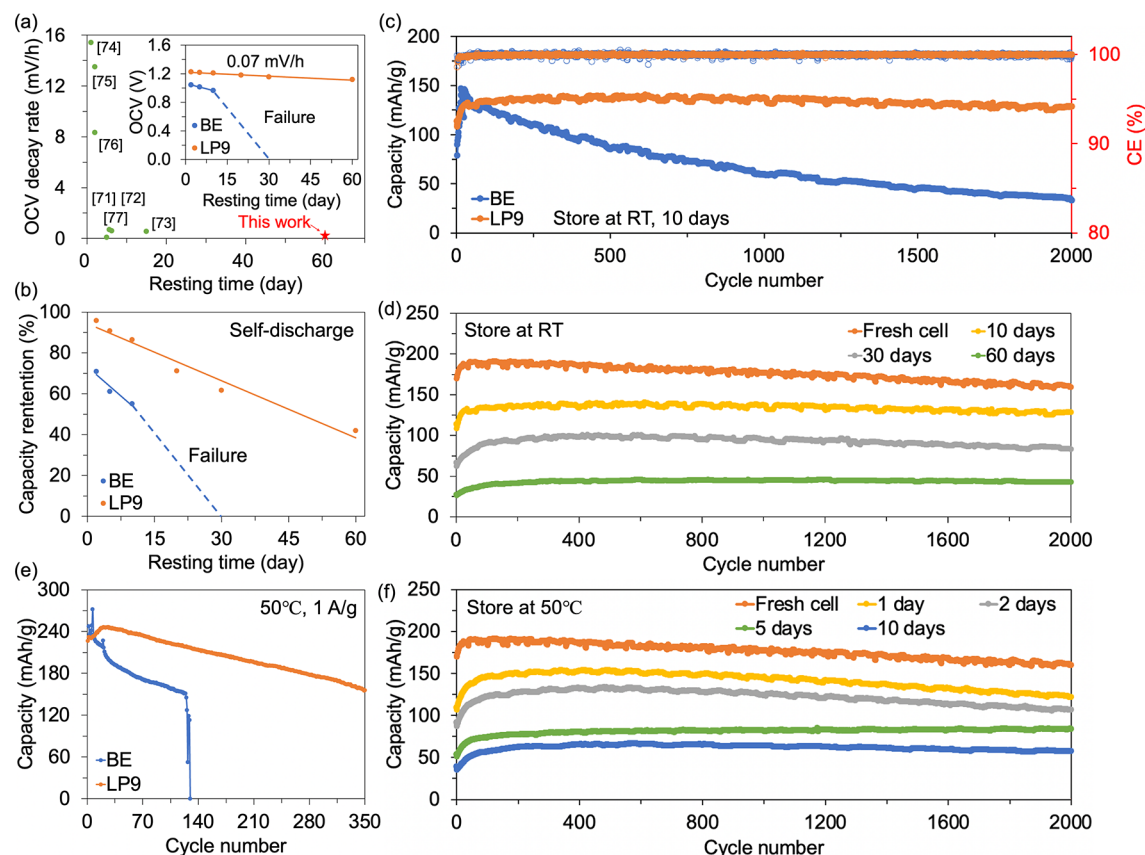
Figure 5. Durability of BE- and LP9-based Zn∥NVO full cells. (a−b) Self-discharge rate determined by the decay of (a) OCV (the figure compares self-discharge rates of previously reported aqueous batteries: Zn-I$_2$ batteries,[71,72] zinc-ion batteries,[73−75] Zn-Br$_2$ batteries,[76] lithium-ion batteries.[77]) and (b) capacity. (c) Cyclic stability of Zn∥NVO full cells after resting at room temperature for 10 days. (d) Cyclic stability of Zn∥NVO full cells after resting at room temperature for up to 60 days. (e) Cyclic stability of Zn∥NVO full cells at 50°C. (f) Cyclic stability of Zn∥ NVO full cells after resting at 50°C for up to 10 days. All of the cycling tests were performed at a charge/discharge current density of 1 A/g.

full cell exhibits a high capacity retention rate of 86.32% after 10,000 cycles. In contrast, the capacity of the BE-based Zn∥ NVO full cell drops dramatically to nearly zero after approximately 5,000 cycles. These results strongly support the effectiveness of the LP9 electrolyte membrane and the exceptional long-term cyclic stability of the separator-free LP9-based batteries at low and high current densities. Moreover, the separator-free LP9-based Zn∥NVO full cells exhibit stable and high average CEs (∼100%) over long-term cycling. The substantially enhanced cyclic stability of the LP9-based Zn∥ NVO full cells strongly supports that the mechanically robust electrolyte membrane with low water activity can effectively suppress water-induced side reactions, thereby enhancing the cyclic stability of Zn∥NVO full cells. As summarized in Table S1, the separator-free LP9-based Zn∥NVO batteries demonstrate superior electrochemical performance in comparison to state-of-the-art AZIBs based on other electrolyte systems with different additives.

To understand the enhanced cyclic stability of the LP9-based Zn∥NVO full cells, the surface morphology of the cycled Zn metal anodes in the full cells was characterized by SEM. As shown in Figure 4f−g, numerous small-sized Zn dendrites and flake-like byproducts are observed on the surface of the Zn metal anode after 1,000 cycles at a current density of 3 A/g in the BE with a GF separator because of inhomogeneous Zn deposition and severe water-induced side reactions. The fibers from the GF separator are embedded by Zn dendrites, ultimately penetrating

the GF separator and causing battery failures. In contrast, Figure 4h−i shows that the Zn metal anode paired with the LP9 electrolyte membrane is free of dendrites after cycling, attributed to the excellent mechanical stiffness of the electrolyte membrane and the uniform Zn deposition during long-term cycling. As presented in Figure 4j, the XRD patterns of the cycled Zn metal anodes reveal that ZHS formation is significantly restricted in the LP9 electrolyte membrane, confirming the effective suppression of water-induced side reactions during long-term cycling.

2.4. Durability of the Separator-Free Zn∥NVO Full Cells. To further investigate the practicality of the LP9 electrolyte membrane, self-discharge tests of the Zn∥NVO full cells were conducted by monitoring their open circuit voltage (OCV) during resting. Figure S23 presents the voltage profiles of the BE- and LP9-based Zn∥NVO full cells. All the cells were charged to 1.4 V and rested for up to 60 days before being fully discharged to 0.4 V. Figure 5a summarizes the OCV of the Zn∥ NVO full cells before discharge. The BE-based Zn∥NVO full cells exhibit rapid voltage decay during resting and experience significant voltage fluctuations after approximately 15 days (Figure S23), suggesting a fast discharge rate and short shelf life of the BE-based batteries, which could be attributed to severe Zn corrosion and HER during long-term resting. For the separator-free LP9-based Zn∥NVO full cells, the voltage primarily drops within the first 5 h (Figure S23). When the resting time is extended from 2 to 60 days, the OCV only drops slightly from

1.2 to 1.1 V, corresponding to a record-low voltage decay rate of 1.7 mV/day or 0.07 mV/h. This value is substantially lower than those of previously reported aqueous batteries,[69,70] as summarized in Figure 5a. Figure 5b shows the capacity retention rates of the Zn‖NVO full cells during the self-discharge tests. After a 2-day resting, the separator-free LP9-based full cell exhibits a capacity retention rate of 95.85%, higher than that (70.89%) of the BE-based full cell. Notably, the LP9-based Zn‖NVO full cells still retain 61.73% and 41.93% of their charge capacities after resting for 30 and 60 days, respectively. These results indicate that the self-discharge rate of the LP9-based Zn‖NVO full cells could be effectively decreased due to the inhibition of water-induced side reactions.

To investigate the influence of resting time on the long-term cyclic stability of the separator-free LP9-based Zn‖NVO full cells, galvanostatic charge/discharge tests were performed. Figure 5c shows the cyclic stability of the aged BE- and LP9-based Zn‖NVO full cells at a current density of 1 A/g. After a 10-day resting, the BE-based Zn‖NVO full cell exhibits an initial capacity of 78.7 mAh/g, significantly lower than that (201.6 mAh/g, Figure 4d) of the fresh BE-based full cell due to the severe Zn corrosion and byproduct formation during resting. In contrast, the aged LP9-based full cell provides an initial capacity of 113.9 mAh/g, and the capacity gradually increases to 139.2 mAh/g after approximately 300 cycles due to electrochemical activation.[29] During the subsequent cycling processes, the capacity slightly decreases to 128.5 mAh/g after 2,000 cycles, which can be attributed to the slight byproduct formation and possible structural degradation of the cathode materials.[78] Figure 5d further demonstrates that the LP9-based Zn‖NVO full cells maintain excellent cyclic stability even after resting for up to 60 days, signifying the long shelf life of the separator-free AZIBs due to the low water activity in the LP9 electrolyte membrane.

The durability of the separator-free LP9-based Zn‖NVO full cells was further investigated at an elevated temperature of 50°C. As shown in Figure 5e, the BE-based Zn‖NVO full cell fails rapidly after 125 cycles at a current density of 1 A/g because of the accelerated dendrite growth and water-induced side reactions. Under the same conditions, the LP9-based Zn‖NVO full cell exhibits a high initial capacity of 226.5 mAh/g and retains 68.65% of its initial capacity after 350 cycles with a high average CE of 99.87% (Figure S24). In addition, the shelf life of the LP9-based Zn‖NVO full cells under elevated temperatures was investigated by resting the fresh cells at 50°C for up to 10 days and then testing them at room temperature. Figure S25 shows that the BE-based full cell fails after resting for 1 day because of the greatly accelerated water-induced side reactions at elevated temperatures. In contrast, as shown in Figure 5f, the LP9-based full cells exhibit outstanding cyclic stability with a high average CE of 99.93% (Figure S26) after being stored at 50°C for 10 days. These results reveal the extraordinary cyclic stability and durability of the separator-free LP9-based Zn‖NVO full cells because of the low water activity and effectively suppressed water-induced side reactions.

3. CONCLUSIONS

In conclusion, a mechanically robust electrolyte membrane based on LP nanoclay is designed for ultrastable and reliable separator-free AZIBs. The outstanding water binding and adsorption capabilities of the LP nanocrystals enabled by the strong water−LP interactions play a crucial role in suppressing water activity. A combination of experimental results and DFT calculations reveals that the water molecules absorbed by LP

nanocrystals are less active in water-induced side reactions, including self-dissociation, byproduct formation, Zn corrosion, and HER. In addition, the LP9 electrolyte membrane eliminates Zn dendrite growth because of its high mechanical resistance and the uniform Zn nucleation/deposition. Consequently, the separator-free LP9-based Zn‖NVO full cells exhibit significantly enhanced cyclic stability with a high capacity retention rate of 94.10% after 2,000 cycles at 1 A/g. At a higher current density of 3 A/g, the LP9-based full cell retains 86.32% of its initial capacity after 10,000 cycles. Furthermore, the separator-free batteries exhibit significantly enhanced durability during long-term storage and improved cyclic stability at an elevated temperature. Because of the low cost and excellent processability, the separator-free LP9-based AZIBs with exceptional safety and reliability exhibit great potential as candidates for large-scale stationary energy storage applications.

4. EXPERIMENTAL SECTION

4.1. Preparation of Electrolytes. The electrolyte membranes were prepared by mixing specific amounts (6−9 g) of laponite (LP) with 10 mL of baseline electrolyte (BE, 2 M ZnSO$_4$ in water). Then, the mixtures were thoroughly stirred at room temperature to form uniform pastes. The as-obtained pastes were further aged for 24 h at room temperature to allow the full hydration and swelling of LP in the electrolyte environments. The resulting electrolyte membranes were denoted as LPx, where x represents the mass of LP per 10 mL of BE. For instance, the electrolyte membranes with 6 and 9 g of LP in 10 mL of BE were denoted as LP6 and LP9, respectively.

4.2. Material Characterization. Scanning electron microscopy (SEM) was conducted on a scanning electron microscope (Sigma 500 VP, Zeiss). The Brunauer−Emmett−Teller (BET) surface area of the materials was determined by a surface area analyzer (Micromeritics ASAP 2020 Plus) via N$_2$ adsorption−desorption isotherms at 77 K. The material structures were analyzed by X-ray diffraction (XRD, Rigaku Ultima IV diffractometer), X-ray photoelectron spectroscopy (XPS, Versa Probe II), Fourier transform infrared spectroscopy (FTIR, Agilent 660), and Raman spectroscopy (NRS-5100, Jasco). The thermal properties were measured by thermogravimetric analysis (TGA, SDT Q600, TA Instruments) at a heating rate of 10 °C/min. The rheological properties of the BE and LP-based electrolyte membranes were measured by a rotational rheometer (Discovery HR-2, TA Instruments) using a stainless steel Peltier plate (8 mm). The ionic conductivities of the BE and LP-based electrolytes were measured by a conductivity meter (EC600, EXTECH).

4.3. Cell Assembling. Standard CR2032 coin cells were used for assembling cells. Zn discs with a thickness of 0.1 mm and a diameter of 14 mm were used as anodes. A glass fiber membrane (GF/A, Whatman) with a diameter of 16 mm was used as separator. The cathode material − sodium-doped vanadium oxide (NVO) − was prepared following the procedures described in prior work.[68] Briefly, 3.638 g of V$_2$O$_5$ and 0.8 g of NaOH were added into 80 mL of ultrapure water under magnetic stirring for 4 h. After that, the solution was transferred to a 200 mL autoclave and kept at 180°C for 48 h. The solid products after hydrothermal treatment were collected and centrifuged with ultrapure water at 5,000 rpm for 15 min, and this was repeated 5 times. The sediments after centrifuge were freeze-dried for 48 h followed by vacuum drying at 80°C for 12 h to obtain the final active materials. The active material (NVO), carbon black, and binder (PVDF) were mixed in a weight ratio of 7:2:1 and ground with NMP to form a slurry. Then, the slurry was uniformly coated on carbon paper (10 × 10 cm^2) and dried under vacuum at 80°C overnight. The mass loading of NVO was 1.5−2 mg/cm^2. Finally, NVO electrodes were obtained by punching the NVO-coated carbon paper into Φ14 mm discs and were used as the cathode for assembling full cells. For BE, 100 μL of liquid electrolytes was used to assemble symmetric and full cells. For the LP-based electrolyte membrane (LP6−LP9), 100 μL of the electrolyte was mechanically compressed into a membrane with a diameter of 16 mm to assemble cells. GF separators were not used for all the LP-based cells.

4.4. Electrochemical Measurements. All of the cells were rested for 2 h before electrochemical tests. The cyclic voltammetry (CV, 0.4−1.4 V), linear sweep voltammetry (LSV), Tafel, chronoamperometry (CA), and electrochemical impedance spectroscopy (EIS, 0.01 Hz to 100 kHz) tests were conducted on an electrochemical workstation (Interface 1010E, Gamry). Among them, Tafel and LSV tests were performed in a three-electrode configuration, in which Pt, Pt, and Ag/AgCl were used as the working, counter, and reference electrodes, respectively. Tafel tests were performed with a voltage window between −300 and 300 mV vs the open circuit potential at a scan rate of 1 mV/s. LSV measurements were carried out at a sweep rate of 5 mV/s from −0.8 to −1.4 V and from 1.2 to 2.0 V to characterize hydrogen and oxygen evolution reactions, respectively. CA tests were performed with an overpotential of −150 mV in a three-electrode configuration, in which Pt, Pt, and Ag/AgCl were used as the working, counter, and reference electrodes, respectively. Galvanostatic charge/discharge tests were performed on a multichannel battery testing system (NEWARE). The Zn^{2+} transference number of the LP9 electrolyte membrane was measured by combining alternating-current (AC) impedance and direct-current (DC) potentiostatic polarization tests using Zn‖Zn symmetric cells. Typically, the electrochemical impedance of the LP9-based Zn‖Zn symmetric cell at the initial state was recorded after resting for 2 h. Then, the cell was polarized under a DC potential of 10 mV for 2,000 s and the response current was recorded. The electrochemical impedance of the symmetric cell was measured immediately after the DC polarization to obtain the steady-state interfacial impedance. The Zn^{2+} transference number ($t_{Zn^{2+}}$) was calculated according to eq 7:

$$t_{Zn^{2+}} = \frac{\Delta V/I_0 - R_0}{\Delta V/I_{ss} - R_{ss}} \tag{7}$$

where ΔV is the applied DC potential. I_0 and I_{ss} are the initial and steady-state response currents under 10 mV of DC polarization, respectively. The interfacial impedance values at the initial state (R_0) and steady state (R_{ss}) are the intersect values of the Z_{real} axis in the Nyquist plots.

4.5. DFT Calculations. The atomic structures of LP were examined using the density functional theory method.[79] The calculations were performed in the Vienna Ab Initio Simulation Package (VASP) implementing the spin-polarized generalized gradient approximation parametrized using the Perdew−Burke−Ernzerhof (PBE) exchange correlation functional.[80] The cut-off energy for the plane wave basis set was 500 eV and a Monkhorst−Pack grid $2 \times 2 \times 1$ k-point was used to model the surface of LP, which was organized from the (001) plane of bulk phyllosilicate $- Na^+_{0.7} [Mg_{5.5}Li_{0.3}Si_8O_{20}(OH)_4]^{-0.7} -$ according to prior work.[40] All the structures were fully relaxed and equilibrated before calculations using the conjugate gradient algorithm by including van der Waals interactions.[81]

4.6. Calculation of the Volume Expansion Ratio of Swelled LP, the Amount of Interlayer Water, and the Salt Concentrations in the LP-Based Electrolyte Membranes. The volume expansion ratio of the swelled LP was calculated by eq 8:[82]

$$\begin{aligned} ER &= \frac{d_{001,swelled} - d_{001,init}}{d_{001,init}} \times 100\% \\ &= \frac{22.8 - 12.5}{12.5} \times 100\% = 82.4\% \end{aligned} \tag{8}$$

where $d_{001,swelled}$ is the basal spacing of LP in the swelled state and $d_{001,init}$ is the initial basal spacing of the LP powder. Therefore, the ratio of the water (RoW) existing within the interlayer spacing can be estimated by eq 9:

$$RoW = (\frac{m_{LP}}{\rho_{LP}} \times ER)/V_{BE} = \left(\frac{9}{2.53} \times 84\%\right)/10 = 29.8\% \tag{9}$$

where m_{LP} and ρ_{LP} are the mass and density of the LP powder, respectively. V_{BE} is the volume of BE (10 mL in this case). Note that a density of 2.53 g/cm³ for LP was used in the calculation according to prior work.[41]

The salt ($ZnSO_4$) concentrations in the LP-based electrolyte membranes were calculated by eq 10:

$$c_{LP} = c_{BE} \times V_{BE}/(V_{BE} + V_{LP}) \tag{10}$$

where c_{LP} and c_{BE} represent the salt concentration in the LP-based electrolyte membranes and the BE, respectively. V_{LP} is the volume of LP, which can be calculated based on its mass and density.

4.7. Quantification of Hydrogen Evolutions during the Soaking Test. A large piece of Zn foil (10×8.7 cm²) was placed in a Petri dish containing 100 mL of BE or LP9 electrolyte. Then the entire Petri dish was tightly sealed with layers of plastic wrap and parafilm to prevent the escape of moisture while allowing the permeation of generated hydrogen gas. The mass of the sealed Petri dish was monitored by an analytic balance with an accuracy of 0.01 mg. The decreased mass of the entire Petri dish represents the mass of the generated hydrogen during the soaking test.

ASSOCIATED CONTENT

ⓈⒾ Supporting Information

The Supporting Information is available free of charge at https://pubs.acs.org/doi/10.1021/acsnano.3c03500.

> SEM image of LP powders, X-ray photoelectron spectroscopy of LP powders, cyclic stability of BE- and LP-based Zn‖NVO full cells, water content in LP-based electrolyte membranes, LP nanocrystals before and after swelling, BET surface area of LP powders, pH of BE and LP-based electrolytes, concentration of $ZnSO_4$ in LP-based electrolyte membranes, SEM images of the LP9 electrolyte membrane, transference number of the LP9 electrolyte membrane, atomic surface models showing H_2O adsorption, Zn^{2+} adsorption energies, Coulombic efficiencies of BE- and LP9-based Cu‖Zn half cells, nucleation overpotential of Zn deposition in BE and LP9 electrolyte, Tafel curves of Zn metal electrodes in BE and LP-based electrolytes, SEM image of bare Zn, SEM images of Zn foil soaked in BE and LP9 electrolyte at 50°C for 10 days, XRD curves of Zn metal soaked in BE and LP9 electrolytes at 50°C for 10 days, long-term cycling performance of Zn‖Zn symmetric cells based on BE and LP-based electrolyte membranes, XRD curves of Zn metal anodes in BE- and LP9-based Zn‖Zn symmetric cells after 30 cycles, cyclic stability of LP9-based Zn‖NVO full cells with different electrolyte volumes, cycling test of BE- and LP9-based Zn‖NVO full cells, voltage profiles of BE- and LP9-based Zn‖NVO full cells during self-discharge tests, CEs of BE- and LP-based Zn‖NVO full cells cycling at 50°C, cyclic stability of a BE-based Zn‖NVO full cell after storing at 50°C for 1 day, CEs of a LP9-based Zn‖NVO full cell after being stored at 50°C for 10 days, summarization of the electrochemical performance of previously reported AZIBs based on different electrolyte additives, and summarization of full cell performance of AZIBs working at high temperatures (PDF)

AUTHOR INFORMATION

Corresponding Authors

    Kyeongjae Cho − *Department of Material Science Engineering, The University of Texas at Dallas, Richardson, Texas 75080, United States;* ⓞ orcid.org/0000-0003-2698-7774; Email: kjcho@utdallas.edu

    Guoping Xiong − *Department of Mechanical Engineering, The University of Texas at Dallas, Richardson, Texas 75080, United States;* Email: guoping.xiong@utdallas.edu

Authors

Siyu Tian — *Department of Mechanical Engineering, The University of Texas at Dallas, Richardson, Texas 75080, United States;* orcid.org/0000-0001-6463-0691

Taesoon Hwang — *Department of Material Science Engineering, The University of Texas at Dallas, Richardson, Texas 75080, United States;* orcid.org/0000-0002-1264-1265

Yafen Tian — *Department of Chemistry & Biochemistry, The University of Texas at Dallas, Richardson, Texas 75080, United States*

Yue Zhou — *Department of Mechanical Engineering, The University of Texas at Dallas, Richardson, Texas 75080, United States*

Long Zhou — *Department of Mechanical Engineering, The University of Texas at Dallas, Richardson, Texas 75080, United States*

Tye Milazzo — *Aerospace and Mechanical Engineering, University of Notre Dame, Notre Dame, Indiana 46556, United States*

Seunghyun Moon — *Aerospace and Mechanical Engineering, University of Notre Dame, Notre Dame, Indiana 46556, United States;* orcid.org/0000-0002-4318-1572

Sina Malakpour Estalaki — *Aerospace and Mechanical Engineering, University of Notre Dame, Notre Dame, Indiana 46556, United States*

Shiwen Wu — *Department of Mechanical Engineering, The University of Texas at Dallas, Richardson, Texas 75080, United States*

Ruda Jian — *Department of Mechanical Engineering, The University of Texas at Dallas, Richardson, Texas 75080, United States*

Kenneth Balkus — *Department of Chemistry & Biochemistry, The University of Texas at Dallas, Richardson, Texas 75080, United States*

Tengfei Luo — *Aerospace and Mechanical Engineering, University of Notre Dame, Notre Dame, Indiana 46556, United States;* orcid.org/0000-0003-3940-8786

Complete contact information is available at:
https://pubs.acs.org/10.1021/acsnano.3c03500

Notes
The authors declare no competing financial interest.

REFERENCES
(1) Ellabban, O.; Abu-Rub, H.; Blaabjerg, F. Renewable energy resources: Current status, future prospects and their enabling technology. *Renewable Sustainable Energy Rev.* **2014**, *39*, 748−764.

(2) Abdalla, A. N.; Nazir, M. S.; Tao, H.; Cao, S.; Ji, R.; Jiang, M.; Yao, L. Integration of energy storage system and renewable energy sources based on artificial intelligence: An overview. *J. Energy Storage* **2021**, *40*, 102811.

(3) Fang, G.; Zhou, J.; Pan, A.; Liang, S. Recent advances in aqueous zinc-ion batteries. *ACS Energy Lett.* **2018**, *3* (10), 2480−2501.

(4) Tang, B.; Shan, L.; Liang, S.; Zhou, J. Issues and opportunities facing aqueous zinc-ion batteries. *Energy Environ. Sci.* **2019**, *12* (11), 3288−3304.

(5) Xie, C.; Li, Y.; Wang, Q.; Sun, D.; Tang, Y.; Wang, H. Issues and solutions toward zinc anode in aqueous zinc-ion batteries: A mini review. *Carbon Energy* **2020**, *2* (4), 540−560.

(6) Verma, V.; Kumar, S.; Manalastas, W., Jr; Srinivasan, M. Undesired reactions in aqueous rechargeable zinc ion batteries. *ACS Energy Lett.* **2021**, *6* (5), 1773−1785.

(7) Yang, W.; Yang, Y.; Yang, H.; Zhou, H. Regulating water activity for rechargeable zinc-ion batteries: Progress and perspective. *ACS Energy Lett.* **2022**, *7* (8), 2515−2530.

(8) Chao, D.; Zhou, W.; Xie, F.; Ye, C.; Li, H.; Jaroniec, M.; Qiao, S.-Z. Roadmap for advanced aqueous batteries: From design of materials to applications. *Sci. Adv.* **2020**, *6*, eaba4098.

(9) Sui, Y.; Ji, X. Anticatalytic strategies to suppress water electrolysis in aqueous batteries. *Chem. Rev.* **2021**, *121* (11), 6654−6695.

(10) Chen, R.; Liu, Q.; Xu, L.; Zuo, X.; Liu, F.; Zhang, J.; Zhou, X.; Mai, L. Zwitterionic bifunctional layer for reversible Zn anode. *ACS Energy Lett.* **2022**, *7* (5), 1719−1727.

(11) Bayaguud, A.; Fu, Y.; Zhu, C. Interfacial parasitic reactions of zinc anodes in zinc ion batteries: Underestimated corrosion and hydrogen evolution reactions and their suppression strategies. *J. Energy Chem.* **2022**, *64*, 246−262.

(12) Xiao, P.; Li, H.; Fu, J.; Zeng, C.; Zhao, Y.; Zhai, T.; Li, H. An anticorrosive zinc metal anode with ultra-long cycle life over one year. *Energy Environ. Sci.* **2022**, *15* (4), 1638−1646.

(13) Lv, Y.; Zhao, M.; Du, Y.; Kang, Y.; Xiao, Y.; Chen, S. Engineering a self-adaptive electric double layer on both electrodes for high-performance zinc metal batteries. *Energy Environ. Sci.* **2022**, *15* (11), 4748−4760.

(14) Hao, J.; Li, X.; Zeng, X.; Li, D.; Mao, J.; Guo, Z. Deeply understanding the Zn anode behaviour and corresponding improvement strategies in different aqueous Zn-based batteries. *Energy Environ. Sci.* **2020**, *13* (11), 3917−3949.

(15) Shin, J.; Lee, J.; Park, Y.; Choi, J. W. Aqueous zinc ion batteries: focus on zinc metal anodes. *Chem. Sci.* **2020**, *11* (8), 2028−2044.

(16) Du, W.; Ang, E. H.; Yang, Y.; Zhang, Y.; Ye, M.; Li, C. C. Challenges in the material and structural design of zinc anode towards high-performance aqueous zinc-ion batteries. *Energy Environ. Sci.* **2020**, *13* (10), 3330−3360.

(17) Tian, S.; Zhou, L.; He, W.; Tian, Y.; Zhou, Y.; Wu, S.; Jian, R.; Balkus, K. J.; Luo, T.; Xiong, G. A self-assembled nanoporous polyelectrolytic interlayer for highly stable zinc metal anodes. *Chem. Eng. J.* **2023**, *462*, 142276.

(18) Chen, J.; Chen, M.; Ma, H.; Zhou, W.; Xu, X. Advances and perspectives on separators of aqueous zinc ion batteries. *Energy Rev.* **2022**, *1*, 100005.

(19) Liu, C.; Xie, X.; Lu, B.; Zhou, J.; Liang, S. Electrolyte strategies toward better zinc-ion batteries. *ACS Energy Lett.* **2021**, *6* (3), 1015−1033.

(20) Zhang, T.; Tang, Y.; Guo, S.; Cao, X.; Pan, A.; Fang, G.; Zhou, J.; Liang, S. Fundamentals and perspectives in developing zinc-ion battery electrolytes: a comprehensive review. *Energy Environ. Sci.* **2020**, *13* (12), 4625−4665.

(21) Tian, S.; Hwang, T.; Malakpour Estalaki, S.; Tian, Y.; Zhou, L.; Milazzo, T.; Moon, S.; Wu, S.; Jian, R.; Balkus, K., Jr; Luo, T.; Cho, K.; Xiong, G. A low-cost quasi-solid-state "water-in-swelling-clay" electrolyte enabling ultrastable aqueous zinc-ion batteries. *Adv. Energy Mater.* **2023**, 2300782.

(22) Chen, M.; Chen, J.; Zhou, W.; Han, X.; Yao, Y.; Wong, C. P. Realizing an all-round hydrogel electrolyte toward environmentally adaptive dendrite-free aqueous Zn−MnO₂ batteries. *Adv. Mater.* **2021**, *33* (9), 2007559.

(23) Sun, P.; Ma, L.; Zhou, W.; Qiu, M.; Wang, Z.; Chao, D.; Mai, W. Simultaneous regulation on solvation shell and electrode interface for

dendrite-free Zn ion batteries achieved by a low-cost glucose additive. *Angew. Chem.* **2021**, *133* (33), 18395−18403.

(24) Meng, R.; Li, H.; Lu, Z.; Zhang, C.; Wang, Z.; Liu, Y.; Wang, W.; Ling, G.; Kang, F.; Yang, Q. H. Tuning Zn-ion solvation chemistry with chelating ligands toward stable aqueous Zn anodes. *Adv. Mater.* **2022**, *34* (37), 2200677.

(25) Han, D.; Wang, Z.; Lu, H.; Li, H.; Cui, C.; Zhang, Z.; Sun, R.; Geng, C.; Liang, Q.; Guo, X. A self-regulated interface toward highly reversible aqueous zinc batteries. *Adv. Energy Mater.* **2022**, *12* (9), 2102982.

(26) Zhang, W.; Dai, Y.; Chen, R.; Xu, Z.; Li, J.; Zong, W.; Li, H.; Li, Z.; Zhang, Z.; Zhu, J.; Guo, F.; Gao, X.; Du, Z.; Chen, J.; Wang, T.; He, G.; Parkin, I. P. Highly reversible zinc metal anode in a dilute aqueous electrolyte enabled by a pH buffer additive. *Angew. Chem. Int. Ed.* **2023**, *62* (5), e202212695.

(27) Hu, Z.; Zhang, F.; Zhao, Y.; Wang, H.; Huang, Y.; Wu, F.; Chen, R.; Li, L. A self-regulated electrostatic shielding layer toward dendrite-free Zn batteries. *Adv. Mater.* **2022**, *34* (37), 2203104.

(28) Zhou, J.; Zhang, L.; Peng, M.; Zhou, X.; Cao, Y.; Liu, J.; Shen, X.; Yan, C.; Qian, T. Diminishing interfacial turbulence by colloid-polymer electrolyte to stabilize zinc ion flux for deep-cycling Zn metal batteries. *Adv. Mater.* **2022**, *34* (21), 2200131.

(29) Cao, J.; Zhang, D.; Yue, Y.; Chanajaree, R.; Wang, S.; Han, J.; Zhang, X.; Qin, J.; Huang, Y. Regulating solvation structure to stabilize zinc anode by fastening the free water molecules with an inorganic colloidal electrolyte. *Nano Energy* **2022**, *93*, 106839.

(30) Gao, J.; Xie, X.; Liang, S.; Lu, B.; Zhou, J. Inorganic colloidal electrolyte for highly robust zinc-ion batteries. *Nano-Micro Lett.* **2021**, *13*, 69.

(31) Zhang, H.; Guo, R.; Li, S.; Liu, C.; Li, H.; Zou, G.; Hu, J.; Hou, H.; Ji, X. Graphene quantum dots enable dendrite-free zinc ion battery. *Nano Energy* **2022**, *92*, 106752.

(32) Zhang, Q.; Luan, J.; Fu, L.; Wu, S.; Tang, Y.; Ji, X.; Wang, H. The three-dimensional dendrite-free zinc anode on a copper mesh with a zinc-oriented polyacrylamide electrolyte additive. *Angew. Chem. Int. Ed.* **2019**, *58* (44), 15841−15847.

(33) Luan, J.; Yuan, H.; Wang, H.; Zhao, N.; Zhong, C.; Lu, J. Nanofluid electrolyte with fumed Al_2O_3 additive strengthening zincophilic and stable surface of zinc anode toward flexible zinc−nickel batteries. *Adv. Funct. Mater.* **2023**, *33* (7), 2210807.

(34) Han, D.; Wang, Z.; Lu, H.; Li, H.; Cui, C.; Zhang, Z.; Sun, R.; Geng, C.; Liang, Q.; Guo, X.; Mo, Y.; Zhi, X.; Kang, F.; Weng, Z.; Yang, Q.-H. A self-regulated interface toward highly reversible aqueous zinc batteries. *Adv. Energy Mater.* **2022**, *12* (9), 2102982.

(35) Stojadinović, J.; Dushina, A.; Trócoli, R.; La Mantia, F. Electrochemical characterization of gel electrolytes for aqueous lithium-ion batteries. *ChemPlusChem* **2014**, *79* (10), 1507−1511.

(36) Chen, S.; Sun, P.; Sun, B.; Humphreys, J.; Zou, P.; Xie, K.; Tao, S. Nitrate-based 'oversaturated gel electrolyte' for high-voltage and high-stability aqueous lithium batteries. *Energy Storage Mater.* **2021**, *37*, 598−608.

(37) Jaumaux, P.; Yang, X.; Zhang, B.; Safaei, J.; Tang, X.; Zhou, D.; Wang, C.; Wang, G. Localized water-in-salt electrolyte for aqueous lithium-ion batteries. *Angew. Chem. Int. Ed.* **2021**, *60* (36), 19965−19973.

(38) Xiao, D.; Dou, Q.; Zhang, L.; Ma, Y.; Shi, S.; Lei, S.; Yu, H.; Yan, X. Optimization of organic/water hybrid electrolytes for high-rate carbon-based supercapacitor. *Adv. Funct. Mater.* **2019**, *29* (42), 1904136.

(39) Liu, X.; Wu, D.; Wang, H.; Wang, Q. Self-recovering tough gel electrolyte with adjustable supercapacitor performance. *Adv. Mater.* **2014**, *26* (25), 4370−4375.

(40) Ruzicka, B.; Zaccarelli, E. A fresh look at the Laponite phase diagram. *Soft Matter* **2011**, *7* (4), 1268−1286.

(41) Cummins, H. Z. Liquid, glass, gel: The phases of colloidal Laponite. *J. Non-Cryst. Solids* **2007**, *353* (41), 3891−3905.

(42) Hensen, E. J. M.; Smit, B. Why Clays Swell. *J. Phys. Chem. B* **2002**, *106* (49), 12664−12667.

(43) Mourchid, A.; Levitz, P. Long-term gelation of laponite aqueous dispersions. *Phys. Rev. E* **1998**, *57* (5), R4887−R4890.

(44) Thompson, D. W.; Butterworth, J. T. The nature of laponite and its aqueous dispersions. *J. Colloid Interface Sci.* **1992**, *151* (1), 236−243.

(45) Kumar, S.; Aswal, V. K.; Harikrishnan, G. Polymer concentration regulated aging in aqueous Laponite suspensions. *Rheol. Acta* **2016**, *55*, 411−421.

(46) Suman, K.; Joshi, Y. M. Microstructure and soft glassy dynamics of an aqueous laponite dispersion. *Langmuir* **2018**, *34* (44), 13079−13103.

(47) Mourchid, A.; Delville, A.; Lambard, J.; LeColier, E.; Levitz, P. Phase diagram of colloidal dispersions of anisotropic charged particles: Equilibrium properties, structure, and rheology of laponite suspensions. *Langmuir* **1995**, *11* (6), 1942−1950.

(48) Dong, M.; Zhang, K.; Wan, X.; Wang, S.; Fan, S.; Ye, Z.; Wang, Y.; Yan, Y.; Peng, X. Stable two-dimensional nanoconfined ionic liquids with highly efficient ionic conductivity. *Small* **2022**, *18* (14), 2108026.

(49) Yan, H.; Li, S.; Nan, Y.; Yang, S.; Li, B. Ultrafast zinc−ion−conductor interface toward high-rate and stable zinc metal batteries. *Adv. Energy Mater.* **2021**, *11* (18), 2100186.

(50) Hao, J.; Yuan, L.; Ye, C.; Chao, D.; Davey, K.; Guo, Z.; Qiao, S. Z. Boosting zinc electrode reversibility in aqueous electrolytes by using low-cost antisolvents. *Angew. Chem. Int. Ed.* **2021**, *60* (13), 7366−7375.

(51) Huo, X.; Xu, L.; Xie, K.; Zhang, K.; Li, J.; Wang, D.; Shu, K. Cation-selective interface for kinetically enhanced dendrite-free Zn anodes. *Adv. Energy Mater.* **2023**, *13*, 2203066.

(52) Mizuno, K.; Miyashita, Y.; Shindo, Y.; Ogawa, H. NMR and FT-IR studies of hydrogen bonds in ethanol-water mixtures. *J. Phys. Chem.* **1995**, *99* (10), 3225−3228.

(53) Chua, R.; Cai, Y.; Lim, P. Q.; Kumar, S.; Satish, R.; Manalastas, W., Jr.; Ren, H.; Verma, V.; Meng, S.; Morris, S. A.; Kidkhunthod, P.; Bai, J.; Srinivasan, M. Hydrogen-bonding interactions in hybrid aqueous/nonaqueous electrolytes enable low-cost and long-lifespan sodium-ion storage. *ACS Appl. Mater. Interfaces* **2020**, *12* (20), 22862−22872.

(54) Jørgensen, P. Infrared study of water adsorbed on Wyoming bentonite. *Geol. fören. Stockh. förh.* **1968**, *90* (2), 213−220.

(55) Zhu, J.; Bie, Z.; Cai, X.; Jiao, Z.; Wang, Z.; Tao, J.; Song, W.; Fan, H. J. A molecular-sieve electrolyte membrane enables separator-free zinc batteries with ultralong cycle life. *Adv. Mater.* **2022**, *34* (43), 2207209.

(56) Zhang, Q.; Ma, Y.; Lu, Y.; Li, L.; Wan, F.; Zhang, K.; Chen, J. Modulating electrolyte structure for ultralow temperature aqueous zinc batteries. *Nat. Commun.* **2020**, *11* (1), 4463.

(57) Chen, W.; Guo, S.; Qin, L.; Li, L.; Cao, X.; Zhou, J.; Luo, Z.; Fang, G.; Liang, S. Hydrogen bond-functionalized massive solvation modules stabilizing bilateral interfaces. *Adv. Funct. Mater.* **2022**, *32* (20), 2112609.

(58) Wang, H.; Ye, W.; Yin, B.; Wang, K.; Riaz, M. S.; Xie, B.-B.; Zhong, Y.; Hu, Y. Modulating cation migration and deposition with xylitol additive and oriented reconstruction of hydrogen bonds for stable zinc anodes. *Angew. Chem. Int. Ed.* **2023**, *135*, e202218872.

(59) Zhou, M.; Guo, S.; Li, J.; Luo, X.; Liu, Z.; Zhang, T.; Cao, X.; Long, M.; Lu, B.; Pan, A.; Fang, G.; Zhou, J.; Liang, S. Surface-preferred crystal plane for a stable and reversible zinc anode. *Adv. Mater.* **2021**, *33* (21), 2100187.

(60) Zhao, Z.; Zhao, J.; Hu, Z.; Li, J.; Li, J.; Zhang, Y.; Wang, C.; Cui, G. Long-life and deeply rechargeable aqueous Zn anodes enabled by a multifunctional brightener-inspired interphase. *Energy Environ. Sci.* **2019**, *12* (6), 1938−1949.

(61) Zeng, Y.; Zhang, X.; Qin, R.; Liu, X.; Fang, P.; Zheng, D.; Tong, Y.; Lu, X. Dendrite-free zinc deposition induced by multifunctional CNT frameworks for stable flexible Zn-ion batteries. *Adv. Mater.* **2019**, *31* (36), 1903675.

(62) Shi, J.; Sun, T.; Bao, J.; Zheng, S.; Du, H.; Li, L.; Yuan, X.; Ma, T.; Tao, Z. Water-in-deep eutectic solvent" electrolytes for high-performance aqueous Zn-ion batteries. *Adv. Funct. Mater.* **2021**, *31* (23), 2102035.

(63) Wang, D.; Li, Q.; Zhao, Y.; Hong, H.; Li, H.; Huang, Z.; Liang, G.; Yang, Q.; Zhi, C. Insight on organic molecules in aqueous Zn-ion batteries with an emphasis on the Zn anode regulation. *Adv. Energy Mater.* **2022**, *12* (9), 2102707.

(64) Blandamer, M. J.; Engberts, J. B. F. N.; Gleeson, P. T.; Reis, J. C. R. Activity of water in aqueous systems; A frequently neglected property. *Chem. Soc. Rev.* **2005**, *34* (5), 440−458.

(65) Scatchard, G. The speed of reaction in concentrated solutions and the mechanism of the inversion of sucrose. *J. Am. Chem. Soc.* **1921**, *43* (11), 2387−2406.

(66) Scatchard, G. The hydration of sucrose in water solution as calculated from vapor-pressure measurements. *J. Am. Chem. Soc.* **1921**, *43* (11), 2406−2418.

(67) Dong, N.; Zhao, X.; Yan, M.; Li, H.; Pan, H. Synergetic control of hydrogen evolution and ion-transport kinetics enabling Zn anodes with high-areal-capacity. *Nano Energy* **2022**, *104*, 107903.

(68) Zhou, J.; Zhang, L.; Peng, M.; Zhou, X.; Cao, Y.; Liu, J.; Shen, X.; Yan, C.; Qian, T. Diminishing interfacial turbulence by colloid-polymer electrolyte to stabilize zinc ion flux for deep-cycling Zn metal batteries. *Adv. Mater.* **2022**, *34* (21), 2200131.

(69) Trócoli, R.; Morata, A.; Erinmwingbovo, C.; La Mantia, F.; Tarancón, A. Self-discharge in Li-ion aqueous batteries: A case study on LiMn$_2$O$_4$. *Electrochim. Acta* **2021**, *373*, 137847.

(70) Suo, L.; Han, F.; Fan, X.; Liu, H.; Xu, K.; Wang, C. Water-in-Salt" electrolytes enable green and safe Li-ion batteries for large scale electric energy storage applications. *J. Mater. Chem. A* **2016**, *4* (17), 6639−6644.

(71) Sonigara, K. K.; Zhao, J.; Machhi, H. K.; Cui, G.; Soni, S. S. Self-assembled solid-state gel catholyte combating iodide diffusion and self-discharge for a stable flexible aqueous Zn−I$_2$ battery. *Adv. Energy Mater.* **2020**, *10* (47), 2001997.

(72) Machhi, H. K.; Sonigara, K. K.; Bariya, S. N.; Soni, H. P.; Soni, S. S. Hierarchically porous metal−organic gel hosting catholyte for limiting iodine diffusion and self-discharge control in sustainable aqueous zinc−I$_2$ batteries. *ACS Appl. Mater. Interfaces* **2021**, *13* (18), 21426−21435.

(73) Zhu, Y.; Yin, J.; Zheng, X.; Emwas, A.-H.; Lei, Y.; Mohammed, O. F.; Cui, Y.; Alshareef, H. N. Concentrated dual-cation electrolyte strategy for aqueous zinc-ion batteries. *Energy Environ. Sci.* **2021**, *14* (8), 4463−4473.

(74) Cui, J.; Wu, X.; Yang, S.; Li, C.; Tang, F.; Chen, J.; Chen, Y.; Xiang, Y.; Wu, X.; He, Z. Cryptomelane-type KMn$_8$O$_{16}$ as potential cathode material—for aqueous zinc ion battery. *Front. Chem.* **2018**, *6*, 352.

(75) Tang, F.; Gao, J.; Ruan, Q.; Wu, X.; Wu, X.; Zhang, T.; Liu, Z.; Xiang, Y.; He, Z.; Wu, X. Graphene-wrapped MnO/C composites by MOFs-derived as cathode material for aqueous zinc ion batteries. *Electrochim. Acta* **2020**, *353*, 136570.

(76) Gao, L.; Li, Z.; Zou, Y.; Yin, S.; Peng, P.; Shao, Y.; Liang, X. A high-performance aqueous zinc-bromine static battery. *Iscience* **2020**, *23* (8), 101348.

(77) Trócoli, R.; Morata, A.; Erinmwingbovo, C.; La Mantia, F.; Tarancon, A. Self-discharge in Li-ion aqueous batteries: A case study on LiMn$_2$O$_4$. *Electrochim. Acta* **2021**, *373*, 137847.

(78) Yang, G.; Li, Q.; Ma, K.; Hong, C.; Wang, C. The degradation mechanism of vanadium oxide-based aqueous zinc-ion batteries. *J. Mater. Chem. A* **2020**, *8* (16), 8084−8095.

(79) Kresse, G.; Furthmüller, J. Efficiency of ab-initio total energy calculations for metals and semiconductors using a plane-wave basis set. *Comput. Mater. Sci.* **1996**, *6* (1), 15−50.

(80) Perdew, J. P.; Burke, K.; Ernzerhof, M. Generalized gradient approximation made simple. *Phys. Rev. Lett.* **1996**, *77* (18), 3865−3868.

(81) Liu, Y.; Merinov, B. V.; Goddard, W. A. Origin of low sodium capacity in graphite and generally weak substrate binding of Na and Mg among alkali and alkaline earth metals. *Proc. Natl. Acad. Sci.* **2016**, *113* (14), 3735−3739.

(82) Suzuki, S.; Prayongphan, S.; Ichikawa, Y.; Chae, B.-G. In situ observations of the swelling of bentonite aggregates in NaCl solution. *Appl. Clay Sci.* **2005**, *29* (2), 89−98.